ACS OMEGA

http://pubs.acs.org/journal/acsodf

Article

Enhancement of Magnetic Surface-Enhanced Raman Scattering Detection by Tailoring Fe_3O_4@Au Nanorod Shell Thickness and Its Application in the On-site Detection of Antibiotics in Water

Leixuri B. Berganza, Lucio Litti,* Moreno Meneghetti, Senentxu Lanceros-Méndez, and Javier Reguera*

Cite This: *ACS Omega* 2022, 7, 45493−45503

Read Online

ACCESS | Metrics & More | Article Recommendations | Supporting Information

ABSTRACT: Surface-enhanced Raman scattering (SERS) has become a promising method for the detection of contaminants or biomolecules in aqueous media. The low interference of water, the unique spectral fingerprint, and the development of portable and handheld equipment for in situ measurements underpin its predominance among other spectroscopic techniques. Among the SERS nanoparticle substrates, those composed of plasmonic and magnetic components are prominent examples of versatility and efficiency. These substrates harness the ability to capture the target analyte, concentrate it, and generate unique hotspots for superior enhancement. Here, we have evaluated the use of gold-coated magnetite nanorods as a novel multifunctional magnetic−plasmonic SERS substrate. The nanostructures were synthesized starting from core-satellite structures. A series of variants with different degrees of Au coatings were then prepared by seed-mediated growth of gold, from core-satellite structures to core−shell with partial and complete shells. All of them were tested, using a portable Raman instrument, with the model molecule 4-mercaptobenzoic acid in colloidal suspension and after magnetic separation. Experimental results were compared with the boundary element method to establish the mechanism of Raman enhancement. The results show a quick magnetic separation of the nanoparticles and excellent Raman enhancement for all the nanoparticles both in dispersion and magnetically concentrated with limits of detection up to the nM range (∼50 nM) and a quantitative calibration curve. The nanostructures were then tested for the sensing of the antibiotic ciprofloxacin, highly relevant in preventing antibiotic contaminants in water reservoirs and drug monitoring, showing that ciprofloxacin can be detected using a portable Raman instrument at a concentration as low as 100 nM in a few minutes, which makes it highly relevant in practical point-of-care devices and in situ use.

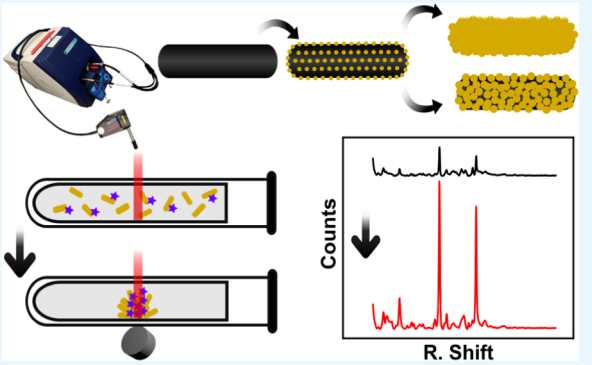

1. INTRODUCTION

Raman scattering is a remarkable analytical technique for the analysis of environmental and biomedical matrices, thanks to the low interference of water and the specific fingerprint of the analyte molecules.[1] However, Raman inelastic scattering is a very inefficient process, limiting its use to applications that do not require low limits of detection. Surface-enhanced Raman scattering (SERS) overcomes the sensitivity drawback, as it extraordinarily enhances the Raman signal when a molecule gets close to a rough metal surface or metal nanoparticle (NP), making this technique an outstanding tool for ultrasensitive analysis.[1−5] Being not only applicable to qualitative analysis but also quantitative analysis, this technique is characterized by its specificity, simplicity, minor or no sample preparation, and minimum amount of sample and use of chemicals in the sample preparation.[6] Besides, the appearance of portable and handheld instruments allows easy in situ analysis of samples with the possibility of the integration of software for the automatic identification of the compounds under analysis.

Among the substrates used in SERS, gold NPs (Au NP) are particularly interesting as the localized surface plasmon resonance (LSPR) takes place in the visible and near-infrared range of the electromagnetic spectrum, which makes it suitable for a large variety of sensing applications, including biomedical ones.[4,5,7] Different from Ag, which usually shows superior Raman enhancement, Au offers unique chemical stability and a wider range of morphologies. Indeed, a large variety of Au NP morphologies have been developed and applied in SERS detection. Although spherical NPs (isotropic) have been largely studied as SERS substrates,[8,9] anisotropic NPs present several advantages, including the capability to tailor the LSPR and the appearance of regions with strong near-field enhance-

Received: September 21, 2022
Accepted: November 17, 2022
Published: November 29, 2022

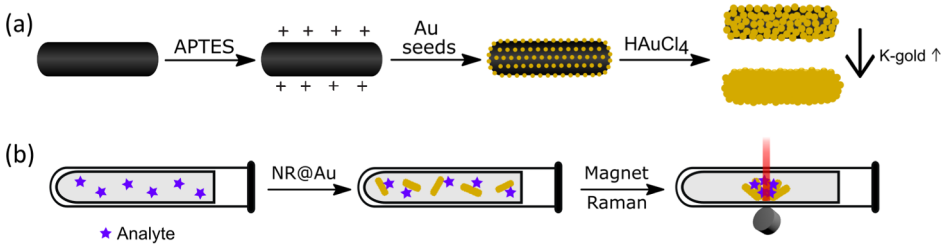

Figure 1. (A) Schematic representation of the synthesis procedure, starting with the solvothermal synthesis of magnetite NRs, which are modified with APTES, then by electrostatic binding of gold nanoclusters, and a final growth of a gold shell. (B) Schematic representation of the measurement procedure, by adding the NR@Au to an antibiotic-containing solution, magnetic separation and accumulation, and Raman measurement at the pellet spot.

ment, a.k.a. intrinsic hotspots, that typically appear at the edges and corners of the NPs.[4] Among the most used anisotropic NPs are nanorods (NRs),[4,10,11] nanostars,[12,13] nanotriangles (nanoplates),[14,15] and nanocubes.[16] Other NPs such as nanoshells have also been explored.[17] In this last case, although the LSPR can be tuned through the shell thickness, they require an assembly to generate extrinsic hotspots. Finally, assemblies of NPs can be also used to generate extrinsic hotspot at the NP junctions.[18,19]

Together with plasmonic NPs, magnetic NPs have been widely applied in analytical applications. They offer the ability to capture, separate, and preconcentrate the analytes at the position where the analytical technique is applied.[20,21] This strategy harnesses the magnetic NP properties to decrease the limits of detection (due to analyte preconcentration) while minimizing or avoiding the matrix effect (due to analyte isolation). In recent years, novel magnetic−plasmonic hybrid NPs have appeared underpinning a multifunctional approach for a unified nanoplatform that can magnetically separate and concentrate the target analytes while offering the plasmonic enhancement required for SERS.[22] Further additional advantages are the guiding and trapping of the NPs at specific locations, for instance, in a microfluidic system, or the generation of higher intensity extrinsic hotspots through the magnetically induced assembly.[23] Finally, magnetic−plasmonic NPs have shown unparalleled versatility to be used in a variety of fields, such as biomedicine, where they can be used in theranostics applications, combining properties such as photothermia, magnetothermia, magnetic guiding, or multimodal contrast agent capabilities.[24−27]

In this context, several approaches for the synthesis of NPs based on iron oxide and gold with different morphologies have also been reported for SERS substrates. Among them, core−shell structures are the most abundant, including here relatively smooth spherical shells[28−32] and spiky/branched shells.[33−37] Other morphologies are, for instance, core-satellite nanostructures,[38−44] Janus NPs,[23,24,45] core-multishell,[46] inverse structures of Au@Fe_3O_4,[47,48] NP aggregates,[49−52] or bigger assemblies.[53−61] Here, we report the use of iron oxide@Au NPs with a novel morphology of the rod core−shell shape as a plasmonic−magnetic SERS substrate. From the plasmonic point of view, this morphology presents hybrid modes of nanoshells and NRs, tunable LSPR through the shell thickness, and hotspots at the NP edges.[62,63] Furthermore, the magnetic rod cores present a ferrimagnetic behavior together with a marked magnetic shape anisotropy.[62,64,65] The NPs were obtained through a seed-mediated-growth method starting from core-satellite NRs, which allows control of the shell thickness and morphology (Figure 1a). This offers the opportunity to study their performance for magnetically manipulable SERS substrates as a function of shell coverage and thickness. Here, the SERS performance of each of the nanostructures was evaluated over the detection of a widely studied model molecule 4-mercaptobenzoic acid (4-MBA),[45,66] in two types of measurements: in colloidal suspension and after magnetic separation and accumulation (Figure 1b). We performed the experiments using portable Raman equipment. It is to notice that portable instruments have far lower performances than the benchtop instrument used in most studies, with limits of detection of more than 15 times higher than benchtop instruments.[67] However, this instrument has shown to be enough for the NPs assayed here and offers higher versatility toward on-site applications. The obtained results were compared with boundary element method (BEM) simulations to further understand the plasmonic behavior of the NPs.

As a proof of concept, the NPs were tested with ciprofloxacin (CIP). CIP is a broad-spectrum fluoroquinolone antibiotic used to treat several bacterial infections such as urinary tract infections or pneumonia.[68] CIP, as a contaminant of emerging concern, has been found on the feces of animals, wastewater, soil, and aquatic ecosystem among others, which raises the alarm for its limitation and monitoring. Continuous and sub-lethal doses encourage genetic changes in bacteria that survive those doses and can lead to antimicrobial resistance.[69,70] In excess, it also can reduce the efficacy of biological nitrogen and phosphorus removal, affect intracellular polyhydroxyalkanoates and glycogen transformation,[71] damage a wide range of organisms,[71,72] or lead to diverse diseases and allergies.[71] Thus, its monitorization is highly relevant both in environmental remediation and monitoring and in improving the comprehension of the dose−effect relationship toward a personalized medicine strategy. Here, its Raman signal was analyzed as a function of the concentration using a portable Raman, underpinning its feasibility to be translated to a point-of-care and in situ analysis.

2. EXPERIMENTAL SECTION

2.1. Materials. Oleic acid 90%, hexadecylamine (HDA) synthesis grade, iron(0) pentacarbonyl, 1-octanol synthesis grade, formaldehyde 37 wt % in H_2O, polyvinylpyrrolidone powder (average $M_w \sim 55{,}000$ g·mol^{-1}), and K_2CO_3 were purchased from Sigma-Aldrich (MERCK). (3-Aminopropyl)-triethoxysilane 98% (APTES), chloroform >99.8%, and hydrogen tetrachloroaurate(III) hydrate 99.9% ($HAuCl_4$) were purchased from Alfa Aesar. Absolute ethanol, EPR Ph.Eur. ≥99.5% V/V, was purchased from Labbox.

https://doi.org/10.1021/acsomega.2c06099
ACS Omega 2022, 7, 45493−45503

Table 1. Amount and Concentration of Fe_3O_4-NR Satellites Added and $HAuCl_4/Fe_3O_4$ Molar Ratio

sample	Fe_3O_4-NR satellites (μL)[a]	Fe (mM)[b]	Au (mM)[b]	Fe (mM)/Au (mM)[c]	Au (mM)[d]	length, L (nm)	width, W (nm)	aspect ratio, AR
NR@Au1	250	0.061	0.993	0.061	3.262	503.5 ± 94.8	250.4 ± 44.1	2.1 ± 0.6
NR@Au2	500	0.115	1.103	0.104	2.334	473.0 ± 36.9	245.0 ± 62.1	2.0 ± 0.4
NR@Au3	1000	0.215	1.185	0.181	1.103	452.9 ± 44.9	172.5 ± 33.7	2.7 ± 0.6
NR@Au4	3000	0.702	1.493	0.470	0.425	407.6 ± 33.1	136.9 ± 25.8	3.0 ± 0.6
NR@Au5	5000	0.912	1.249	0.734	0.272	384.9 ± 61.6	90.6 ± 32.6	4.6 ± 1.3
NR@Au6	10,000	1.283	1.321	0.971	0.137	372.8 ± 78.4	67.6 ± 9.7	5.6 ± 1.5

[a]Amount of Fe_3O_4-NR satellites added to K-gold solution. [b]Final iron and gold sample concentrations. [c]Iron/Au final ratio. [d]Gold concentration of samples for SERS measurements (Fe = 0.2 mM).

2.2. Synthesis. The synthesis was performed based on our previously published method.[62] Magnetite NRs were synthesized by the solvothermal method. HDA (0.71 g) and 5.33 mL of oleic acid were dissolved in 21.33 mL of 1-octanol at 40 °C under magnetic stirring until a homogeneous solution was obtained. Then, after the solution cooled down to room temperature, 5.33 mL of $Fe(CO)_5$ was added and stirred for 2 min. Then, the mixture was transferred to a 50 mL Teflon-lined autoclave, sealed with its stainless-steel shell, and heated at 200 °C for 6 h, without a heating ramp and after preheating the oven. After cooling to room temperature, the product was washed three times with ethanol and dispersed in 10 mL of chloroform (26.4 mg·mL^{-1}).

The well-dispersed NR solution (100 μL) was added drop by drop into a solution of 600 μL of APTES and 5 mL of ethanol and mixed using a rotary tube mixer overnight. Then, the NRs were washed twice with ethanol and dispersed in 3 mL of ethanol. On the other side, spherical Au NPs (2−3 nm) were synthesized in parallel. For that, 1.8026 g of PVP was dissolved in 100 mL of ultrapure H_2O, and then 428 μL of a solution of $HAuCl_4$ (100.36 mM) was added to the solution. NPs were finally formed by adding 30 mL of $NaBH_4$ solution as a reducing agent (5.24 mM) and left for a few minutes to react. The NP solution was then stored in the fridge until further use.

The APTES-functionalized NRs (3 mL) were added drop by drop into 30 mL of Au NP solution and mixed with a rotary tube mixer for 2 h. The resulting core-satellite NRs were purified by centrifugation and dispersed in water. This process was repeated once more to improve the satellite coating of the NRs.

For the Au shell coating, a K-gold solution was prepared as a gold growing solution. For that, 0.0264 g of K_2CO_3 was dissolved in 105.86 mL of ultrapure H_2O for 15 min under magnetic stirring. Then, 265.6 μL of $HAuCl_4$ solution (149.1 mM) was added and mixed for 30 min, where the solution becomes colorless because of the reduction of Au^{3+} to Au^{+}. The solution (250−10,000 μL) of Fe_3O_4-NR satellites (Fe_3O_4 = 4.73 mM; Au = 0.25 mM) was added under orbital stirring (see Table 1) to 106 mL of K-gold solution. Finally, after 1 min, 260 μL of formaldehyde was added as a reducing agent. After 2 h, the reaction was completed, and no change was further observed in the ultraviolet−visible (UV−vis) spectrum. The NPs were then purified by centrifugation twice and dispersed in 25 mL of water.

2.3. Characterization Methods. *2.3.1. Transmission Electron Microscopy.* Transmission electron microscopy (TEM) images were acquired in a JEOL JEM-1400 PLUS instrument operating at 100 kV after NPs were deposited on a carbon-coated TEM grid. The NP morphological features were analyzed with the ImageJ software package.

2.3.2. UV−Vis Spectroscopy. The absorbance of NP solutions was recorded using a Cary 60 (Agilent) over the 300−1100 nm range in a standard Macro cuvette using diluted aqueous solutions.

2.3.3. Surface-Enhanced Raman Spectroscopy. SERS measurements were performed using a Raman portable instrument (iRaman Plus, BWTEK), using a 785 nm excitation laser and equipped with a microscope accessory. The amount of iron oxide of all nanostructures was dosed according to the Fe content, so that the same amount of particles, despite different Au coverages, was used for all measures. 0.2 mM Fe (4.69×10^9 NPs/mL) of the core@shell structures was therefore mixed with analytes of study (MBA or CIP). After 15 min, 15 μL of this mixture was then inserted in 1 mm glass capillary and mounted on a hand-made holder that allows locating the capillary and the magnet under the microscope of the portable Raman. For measurements of magnetically accumulated samples, a neodymium magnetic disc, 10 nm in diameter and 4 mm height (380 mT), was placed below the capillary forming approximately 45° angle, so NPs could accumulate close to the magnet edge forming a small line instead of a bigger area. SERS spectra were then measured after 15 min of accumulation. For measurements of samples in suspension, the same holder without the magnet was used. All SERS spectra were collected using a 10 objective magnification (numerical aperture NA = 0.25) with an integration time of 50 s and a laser power of about 5 mW. All spectra were treated by correcting the background using MATLAB R2020b software and smoothing with Origin 8.5 software.

2.4. Simulations. Simulations were run using the BEM by the related libraries developed by Hohenester in the MATLAB environment.[73] Enhanced local fields were calculated by exciting at 785 nm, propagating, and polarizing along x, y, and z, according to previously published methodologies.[74,75]

2.5. SERS Enhancement Factor Calculation. The enhancement factor (EF) was calculated according to the following formula (eq 1)[75]

$$\mathrm{EF} = \frac{\frac{I_{\mathrm{SERS}}}{N_{\mathrm{SERS}}}}{\frac{I_{\mathrm{Raman}}}{N_{\mathrm{Raman}}}} \quad (1)$$

where I_{SERS} and I_{Raman} are the intensity, or count number, received by the instrument under the same conditions, for SERS and Raman, respectively. This intensity was weighed by the laser power used and time, which can be different for the Raman and SERS measurements. N_{SERS} and N_{Raman} are the number of molecules measured for SERS and Raman, respectively. Given a certain laser focus volume (V_f), the number of molecules will be V_f multiplied by the concentration (C). For the case of SERS, this value was taken as proportional to the concentration of the analyte in the solution, while in the

https://doi.org/10.1021/acsomega.2c06099
ACS Omega 2022, 7, 45493−45503

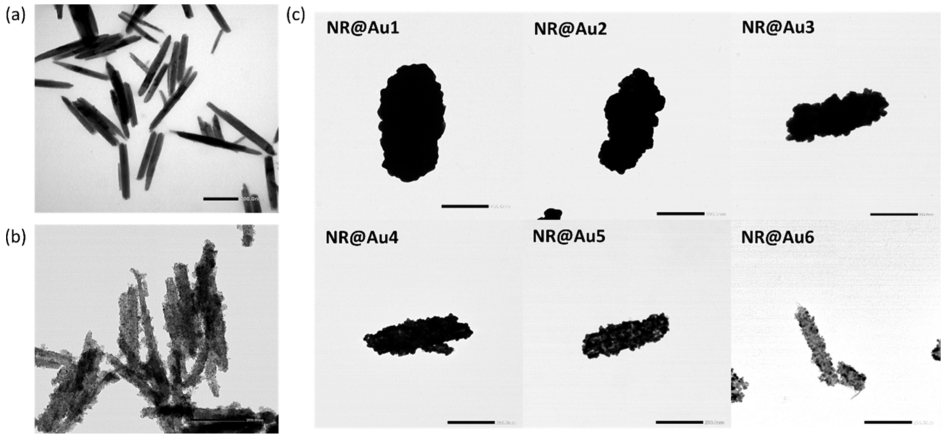

Figure 2. a) TEM image of Fe_3O_4 NRs. (b) TEM image of the NR core-satellite structure. (c) TEM images of core@shell structures synthesized by adding different amounts of Fe_3O_4-NR satellites: NR@Au1 250 μL, NR@Au2 500 μL, NR@Au3 1000 μL, NR@Au4 3000 μL, NR@Au5 5000 μL, and NR@Au6 10,000 μL, from the thickest (NR@Au1) to the least complete (NR@Au6). The scale bar corresponds to 200 nm.

case of Raman, due to its low signal, the experiment was performed as a solid, and the concentration was calculated by its density and molecular weight.

3. RESULTS AND DISCUSSION

Figure 1a represents the different steps followed in the synthesis of the multicomponent core@shell Fe_3O_4@Au NRs exhibiting ferromagnetic and plasmonic behavior. Figure 2A shows the representative TEM image of the initial magnetite NRs synthesized by the solvothermal method in 1-octanol using iron pentacarbonyl as the iron source and oleic acid and HDA as capping ligands. The size of the NRs can be controlled by the amount of HDA added to the synthesis.[62] For this work, relatively large NRs were selected (length = 378.8 ± 56.1 nm, width = 42.2 ± 6.9 nm, and AR = 89.2 ± 2.1) to promote a good formation of the Au shell while maintaining a high aspect ratio for thick shells and high magnetic volume for fast magnetic accumulation.[76] This synthesis gives rise to iron oxide NRs, mainly single-crystal morphologies of magnetite, as previously reported by high-resolution TEM, X-ray diffraction, and X-ray photoelectron spectroscopy.[62]

Once the magnetite NRs were synthesized, the Au coating was carried out following a multistep approach (see Section 2.2). After silanization with APTES and transfer to a water phase, Au nanospheres (<3 nm) were electrostatically bound to form NR core@satellite (NR-satellite) structures that act as seeds for further growth of gold (Figure 2b). The growth of gold was carried out from a K-gold growing solution in the presence of a reducing agent. The gold grows on top of these satellites and finally merges to form a complete shell surrounding the magnetite core. Figure 2c (1−6) shows representative TEM images of the different core@satellites and core@shell structures synthesized following this process. Shell growth was controlled by adjusting the ratio between NR-satellites seeds and K-gold growing solution (see Table 1 in Section 2.2). Satellites act as autocatalytic growing sites, so that the gold layer grows more when the proportion of satellites with respect to K-gold solution is lower, obtaining shells with different morphologies: from the complete and thicker one, NR@Au1 (length = 503.5 ± 94.8 nm, width = 250.4 ± 44.1 nm, and AR = 2.1 ± 0.6), to the least complete and thinner, NR@Au6 (length = 372.8 ± 78.4 nm, width = 67.6 ± 9.7 nm, and AR = 5.6 ± 1.5). As shown in Figure 2, complete shells were only obtained for NR-Au1, NR-Au2, and NR-Au3 with different thicknesses of shell, while the satellite structure is still visible for the other samples, indicating a partially coated surface. Finally, Figures S1−S7 show low-magnification TEM images of the synthesized NPs, with a high number of coated NPs together with a few NPs with other morphologies, mainly spheres, and a few aggregates.

Figure 3 shows the UV−vis spectra of all the six synthesized nanostructures. These spectra correspond to the light

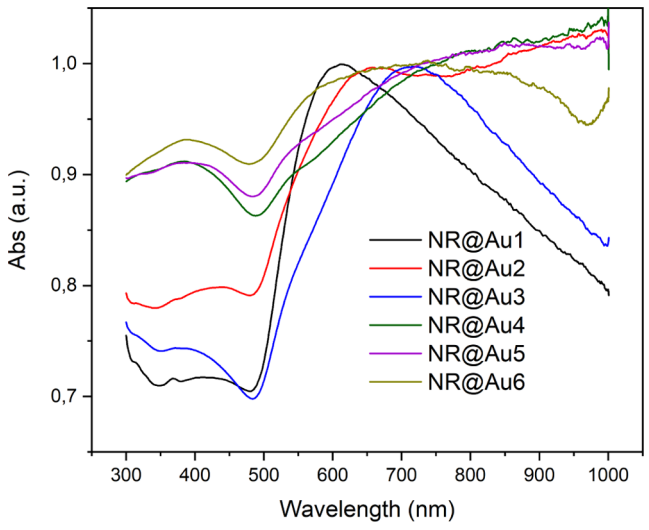

Figure 3. Representative UV−vis spectra of the synthesized NPs described in Figure 1.

extinction which will be composed to an absorption component and a scattering component, which cannot be measured in a standard UV−vis spectrophotometer but is not negligible, although it takes place in a similar range of wavelengths, and should be taken in consideration when describing the system.[77] Typically, plasmonic NR shells show two plasmon bands on their UV−vis spectra, which correspond to transverse and longitudinal hybrid dipolar modes.[63] The transversal hybrid mode is present in all NPs as a shoulder at 500−550 nm. Regarding the lower energy longitudinal hybrid modes, the first three core−shell structures, NR@Au1, NR@Au2, and NR@Au3, present an LSPR band centered at ∼600,

https://doi.org/10.1021/acsomega.2c06099
ACS Omega 2022, 7, 45493−45503

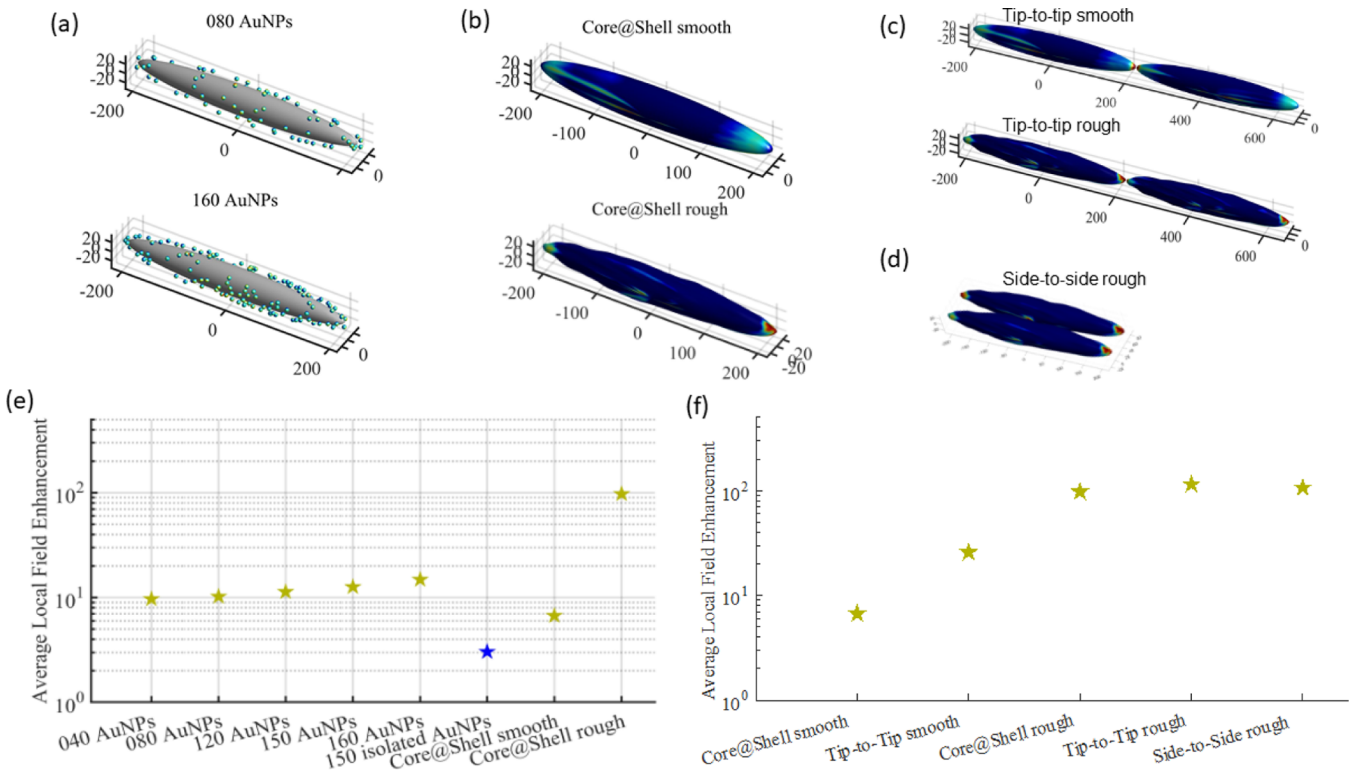

Figure 4. BEM simulations of several morphology configurations: (a) Fe_3O_4 NRs functionalized with different amounts of Au nanospheres; (b) smooth (top) and rough (bottom) core@shell Fe_3O_4@Au NRs; (c) tip-to-tip assembled smooth (top) and rough (bottom) core@shell structures; (d) side-to-side assembled rough core@shell structures; (e) average local field enhancements of the different nanostructures (Fe_3O_4 NRs functionalized with different amounts of Au nanospheres randomly located, isolated Au nanospheres, and smooth and rough core@shell structures); and (f) average local field enhancement tip-to-tip assemblies of smooth and rough core@shell NRs compared with the individual ones.

~650, and ~700 nm respectively. The decrease in wavelength with the shell thickness is due to the change in hybrid plasmonic modes, considering a rod shape cavity and a solid rod, and has been already described for nanorice particles (gold-coated hematite prolate spheroids).[63] This, in fact, shares similar blue-shift trends to spherical nanoshells with increasing thickness[78] and Au NRs with a decrease in aspect ratio.[79] The band of NR@Au2 is broader than the other two with extension to higher wavelengths, probably due to some small aggregation during the synthesis and its more irregular shape. In the case of non-complete shells, NR@Au4 and NR@Au5 present a broad absorption peak between ~600 and 1100 nm and NR@Au6 between ~600 and 900 nm. These bands could be attributed to the more complex structure of the partial shell where part of the satellites has already merged, giving rise to additional plasmonic modes at these irregularities.[75] Finally, the relative absorbance A_{max}/A_{400nm}, indicative of the total extinction coefficient (A_{400nm} is proportional to the amount of Au),[80] tends also to increase with the size of the shell, suggesting more uniform plasmonic modes.

To further understand the behavior of the synthesized core−shell NRs upon their use in SERS, BEM simulations were carried out to determine the near-field enhancement in respect of the density of satellites and shell homogeneity (Figure 4). First, these simulations were obtained by magnetite NRs functionalized with Au nanospheres at different amounts and randomly positioned (Figure 4a). As more NPs were added, the packing became denser, which increased the probability of building up effective hotspots between the AuNPs. As expected, the higher coverage of the surface increased the proximity of spheres and therefore increased both average and maximum local field enhancement (Figure 4e). This part would be somehow analogous to the growth of the spheres for samples NR@Au1 and NR@Au2, where a decrease in distance between spheres is also produced. Although not simulated here, it is expected that the merge of nanospheres, especially for further growth, would also create new hotspots, which would contribute to the enhancement of the near electromagnetic field. Interestingly, a uniform and 50 nm-spaced AuNP assembly (high number of particles but well separated) does not develop the same local field enhancements as the relative core@satellite system (Figure 4e) as the proximity among Au NPs is the main parameter to form such hotspots, and it is much more important than simply the overall Au NP number.

For a complete shell, two situations were simulated, a smooth and a rough homogeneous core@shell structure (Figure 4b). As shown in Figure 2, the rough shell is the closest to the real samples due to the synthesis method that produces small protrusions where the initial satellites were located. The smooth core−shell has a limited average local field enhancement (Figure 4e) because of the formation of hotspots restricted to the edges of the NR-shaped particles. On the other hand, the rough core−shell structure presents a much higher local field enhancement than the rest of the structures (Figure 4e), arising from the combination of the hotspots at the NR edges and at the protuberances of the rough surface.

Together with the intrinsic hotspots observed for the core−shell NRs, new hotspots emerge by the assembly of these NPs.

https://doi.org/10.1021/acsomega.2c06099
ACS Omega 2022, 7, 45493−45503

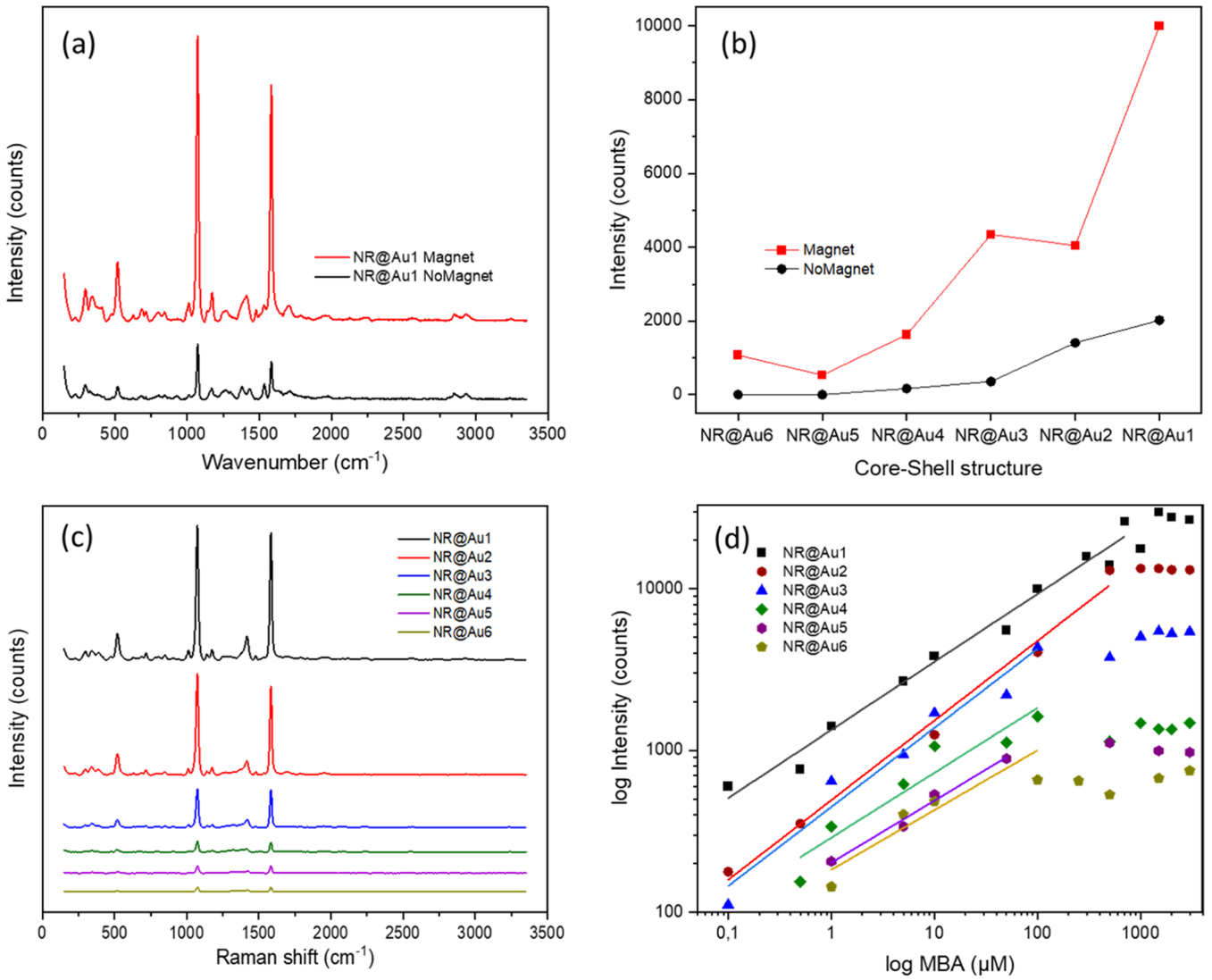

Figure 5. (a) Raman spectra of MBA (0.1 mM) measured using a magnet and without it. (b) Intensity of the first characteristic peak of MBA (1072 cm^{-1}) at 0.1 mM with each core−shell structure using a magnet and without it. (c) Raman spectra of MBA (1 mM) performed with each of the core−shell structure. (d) Intensity of the first characteristic peak of MBA (1072 cm^{-1}) at different concentrations measured with each core@shell structure.

This is highly relevant due to the dual functionality of these particles that enables magnetic separation and concentration. Due to the magnetization of the NRs in the easy axis direction, which corresponds to the geometrical axis, an abundance of tip-to-tip configurations is expected.[81] Moreover, as has been observed for Au NRs, this configuration could give rise to very intense hotspots.[82] Therefore, tip-to-tip assembled core@shell rough and smooth structures were simulated (Figure 4c, where the colormaps are set at a maximum of 10^2 local field enhancement for clarity of comparison). For the case of the smooth shell, when it is tip-to-tip assembled, a net local field accumulation is observed at the rod junction, in respect of the isolated single rod. The results are different for the case of the more realistic rough shell structures, where a lower increase in the average local field enhancement was observed for tip-to-tip assembled structures with respect to the individual one (Figure 4f). This is probably due to the plasmonic nature of the rough nanostructure already rich in intrinsic hotspots, especially at the region characterized by the highest curvature, that is, the tips. In addition, a magnetic assembly could also give rise to side-to-side configurations by the assembly of rows of NRs. Figure 4d shows this configuration for rough NRs. Interestingly, it shows a similar EF (Figure 4f) to the tip-to-tip configurations or individual rough NRs, pointing out the high relevance of surface roughness in the plasmonic behavior of these NPs. On the whole, the generated extrinsic hotspots correspond to similar gain. This differs quite dramatically from other spherical core−shell nanostructures, which do not present intrinsic hotspots and require the assembly to form extrinsic ones and generate a relatively high SERS signal.[83]

The SERS performance of the synthesized nanostructures was evaluated using 4-MBA as a model molecule (Figure 5). All measurements were performed using the same concentration in the number of NPs, 4.69×10^9 NPs/mL (i.e., maintaining a Fe concentration of 0.2 mM), to make a proper comparison among different measurements. At first, the magnetic separation was assayed by measuring both in colloidal solution and after magnetic separation/concentration (Figure 5a). The magnetic concentration was produced by placing a small magnet close to the glass capillary surface (as

https://doi.org/10.1021/acsomega.2c06099
ACS Omega 2022, 7, 45493−45503

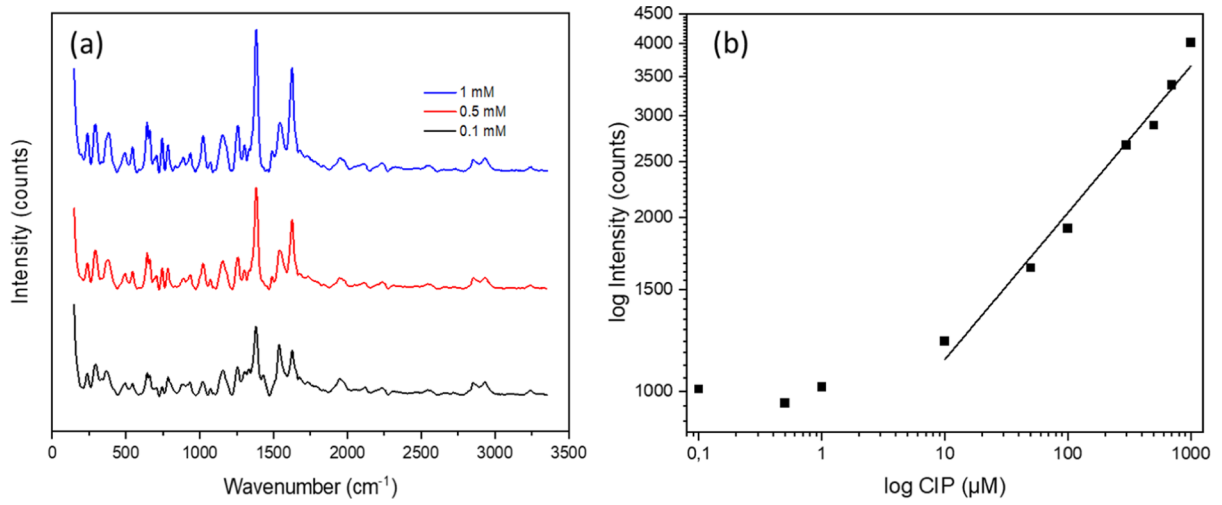

Figure 6. (a) Raman spectra of CIP at different concentrations using NR@Au1 as the substrate. (b) Intensity of one characteristic peak of CIP (1382 cm^{-1}) at different concentrations performed with the NR@Au1 structure.

schematically depicted in Figure 1B). A dense spot of NPs was produced in less than 15 min. This rapid separation, in comparison with other systems,[45] was enabled, thanks to the relatively large size of the NPs, which generates a high magnetization and therefore a high attraction force. The SERS measurement was produced by focusing the exciting laser at that spot. Figure 5a shows an example of that measurement using NR@Au1 as the SERS substrate. As a result of the magnetic concentration, the intensity of the signal was several times higher than the one in the solution.

As discussed before in the BEM simulation, the assembly of the NRs and the generation of new hotspots are probably not the main causes of intensity gain in this situation as far as the particles themself already present bright hotspots. Thus, the higher SERS signals due to the magnetic attraction are expected to be caused by the capture of the analyte on the NP surface and accumulation at the laser spot. It generates an analyte-rich region that indeed produces a signal gain as high as 1 order of magnitude for the characteristic peak of MBA at 1072 cm^{-1} (Figure 5a,b).

To evaluate the SERS efficiency, the EF was calculated according to the formula (eq 1). In the case of the best performing structure, NR@Au1, 6×10^4 EF is achieved for NPs in dispersion, which is further increased to 3×10^5 EF when the NPs are magnetically concentrated. Note here that although EF values are in line with other systems,[35,52,84] most of them were performed with a benchtop instrument, therefore lacking the flexibility of a portable instrument.

To compare the SERS performances of different core@shell structures and to provide evidence about the effectiveness of this setup for quantitative SERS analysis using a portable Raman instrument, a more complete investigation was performed by recovering calibration curves under magnetic accumulation. Figure 5c shows SERS spectra of MBA at 1 mM using each core@shell structure as the substrate. A very clear monotonic increase in intensity versus the Au-shell coverage is appreciated. Figure 5d represents the intensity of the first characteristic peak at 1072 cm^{-1} at different concentrations. A higher intensity appears as the MBA concentration increases up to a saturation concentration for all samples of the series. At saturation, a similar monotonic trend of the core@shell structure series is found. A higher amount of gold (NR@Au1) reports higher SERS intensities along all the curves and a higher MBA saturation concentration. These results are in agreement with the trend observed in the simulations, where the SERS performance is directly related to the amount of gold coverage (Figure 5d), achieving the lowest signal with the less complete shell (NR@Au6) and the highest with the thickest of the complete shells (NR@Au1). The lowest limit of detection (LOD), achieved with NR@Au1, was on the nanomolar regime (50 nM, corresponding to 750 fmols of MBA). For values lower than the saturation, the results can be fit to a linear function (Figure 5d), allowing its quantitative analysis.

Given the abovementioned results, NR@Au1 was selected as the best SERS performing structure, and it was used to detect CIP in water samples. CIP presents amines and carboxylate groups in addition to an extended aromatic cycle, which makes it suitable for binding to the gold surface. Figure 6a shows SERS spectra of CIP collected at different concentrations. The more prominent signals are at 1382 and 1624 cm^{-1} which correspond to the carboxylic and aromatic stretching modes, respectively.[75]

Figure 6b shows the intensity of the highest intensity peak of CIP (1382 cm^{-1}) at different concentrations until no signal was detected. On the other end, at high concentrations, the measurements were limited up to the solubility of CIP, so the calibration curve was performed only up to 1 mM. The lowest concentration detected was in the sub-micromolar regime (100 nM, 1.5 pmols), while the lowest concentration that could be quantified was 10 μM, making it suitable for the detection of subinhibitory concentrations of CIP in water reservoirs.[85] CIP concentrations are toxic at much higher concentrations, for instance, LC_{10} in zebrafish is 5.9 mM,[86] while inhibition of mexican freshwater algae growth is around 0.12 M,[72] in line with other aquatic organisms[87,88] On the other hand, the worldwide median concentration of CIP in the freshwater ecosystem has been reported to be 0.164 mg/L (4.9×10^{-4} mM) and the maximum 6.5 mg/L (2.0×10^{-2} mM),[72] also above the detection limit of this system.

Calibration curves were obtained with each substrate and analyte, probing the potential of the method for quantitative purposes,[89] as Table 2 shows, where the linear regression parameters and detection limits have been summarized for each analyte and substrate.

https://doi.org/10.1021/acsomega.2c06099
ACS Omega 2022, 7, 45493−45503

Table 2. SERS Quantification/Calibration Parameters after Linear Fit in the Log−Log Plot

		regression fit $\log(I) = a + b \cdot \log C$			
analyte	NPs	a	b	R^2	LOD[a] (nM)
MBA	NR@Au1	3.124 ± 0.036	0.419 ± 0.020	0.981	50
MBA	NR@Au2	2.691 ± 0.047	0.491 ± 0.029	0.989	100
MBA	NR@Au3	2.649 ± 0.065	0.487 ± 0.052	0.956	500
MBA	NR@Au4	2.459 ± 0.077	0.399 ± 0.064	0.906	500
MBA	NR@Au5	2.304 ± 0.036	0.383 ± 0.034	0.984	1000
MBA	NR@Au6	2.261 ± 0.127	0.368 ± 0.098	0.823	1000
CIP	NR@Au1	2.801 ± 0.039	0.254 ± 0.017	0.978	100

[a]Limit of detection.

4. CONCLUSIONS

It has been proven that multicomponent NPs of gold and magnetite with a core−shell-rod morphology can be applied as colloidal SERS sensing substrates with magnetic capture and concentration. While the synthesis method allows the formation of NPs with partial shells and therefore with intrinsic hotspots, the performance was better for a complete shell with rough surfaces with a monotonic increase in signal with the increase in gold thickness. Moreover, the enhancement highly increased with the magnetic concentration, with respect to colloidal dispersion, which is ascribed to a higher increase in analytes in the Raman measurement region instead of the generation of new extrinsic hotspots. Finally, quantitative calibration curves were obtained with these NPs with 4-MBA and the antibiotic CIP in water and using a portable Raman. Limits of detection as low as 50 nM for 4-MBA and 100 nM for CIP were obtained, opening the path for in situ detection of contaminants or in point-of-care biomedical applications.

■ ASSOCIATED CONTENT

Supporting Information

The Supporting Information is available free of charge at https://pubs.acs.org/doi/10.1021/acsomega.2c06099.

TEM images of core-satellite and core−shell NPs (PDF)

■ AUTHOR INFORMATION

Corresponding Authors

Lucio Litti − *Nanostructures and Optics Laboratory, Department of Chemical Sciences, University of Padova, 35131 Padova, Italy;* orcid.org/0000-0001-6247-5456; Email: lucio.litti@unipd.it

Javier Reguera − *BCMaterials, Basque Center for Materials, Applications, and Nanostructures, UPV/EHU Science Park, 48940 Leioa, Spain;* orcid.org/0000-0001-5110-5361; Email: javier.reguera@bcmaterials.net

Authors

Leixuri B. Berganza − *BCMaterials, Basque Center for Materials, Applications, and Nanostructures, UPV/EHU Science Park, 48940 Leioa, Spain*

Moreno Meneghetti − *Nanostructures and Optics Laboratory, Department of Chemical Sciences, University of Padova, 35131 Padova, Italy;* orcid.org/0000-0003-3355-4811

Senentxu Lanceros-Méndez − *BCMaterials, Basque Center for Materials, Applications, and Nanostructures, UPV/EHU Science Park, 48940 Leioa, Spain; Ikerbasque, Basque Foundation for Science Bilbao, 48009 Bilbao, Spain;* orcid.org/0000-0001-6791-7620

Complete contact information is available at: https://pubs.acs.org/10.1021/acsomega.2c06099

Author Contributions

L.B.B. performed the investigation, the formal analysis of the data, and the writing of the original draft. L.L. performed the BEM simulations and formal analysis of the data. J.R. and L.L. performed the conceptualization, designed the methodology, reviewed and edited the original draft, and supervised the work. J.R. performed the project administration. M.M. and S.L.-M. provided the resources and reviewed the work.

Notes

The authors declare no competing financial interest.

■ ACKNOWLEDGMENTS

This work has been funded by the Spanish State Research Agency (AEI) through the project PID2019-106099RB-C43/AEI/10.13039/501100011033 and the Basque Government Industry and Education Departments under the ELKARTEK program, KK-2021/00124. The authors thank the technical and human support provided by SGIker (UPV/EHU/ERDF, EU). L.L. and M.M. thank the Interdepartmental Center for Research, Study and Conservation of Archaeological, Architectural and Historical-Artistic Heritage (CIBA), at the University of Padova, for the portable Raman instrument. L.L. and L.B.B. also acknowledge the European Commission and Regione Veneto for POR FSE 2014-2020 ID 2105-0043-1463-2019 as financial support for the project.

■ REFERENCES

(1) Lindquist, N. C.; Nagpal, P.; McPeak, K. M.; Norris, D. J.; Oh, S.-H. Engineering Metallic Nanostructures for Plasmonics and Nanophotonics. *Rep. Prog. Phys.* **2012**, *75*, 036501.

(2) Managò, S.; Tramontano, C.; Delle Cave, D.; Chianese, G.; Zito, G.; De Stefano, L.; Terracciano, M.; Lonardo, E.; De Luca, A. C.; Rea, I. SERS Quantification of Galunisertib Delivery in Colorectal Cancer Cells by Plasmonic-Assisted Diatomite Nanoparticles. *Small* **2021**, *17*, 2101711.

(3) Hussain, A.; Sun, D. W.; Pu, H. Bimetallic Core Shelled Nanoparticles (Au@AgNPs) for Rapid Detection of Thiram and Dicyandiamide Contaminants in Liquid Milk Using SERS. *Food Chem.* **2020**, *317*, 126429.

(4) Reguera, J.; Langer, J.; Jiménez de Aberasturi, D.; Liz-Marzán, L. M. Anisotropic Metal Nanoparticles for Surface Enhanced Raman Scattering. *Chem. Soc. Rev.* **2017**, *46*, 3866−3885.

(5) Langer, J.; Jimenez de Aberasturi, D.; Aizpurua, J.; Alvarez-Puebla, R. A.; Auguié, B.; Baumberg, J. J.; Bazan, G. C.; Bell, S. E. J.; Boisen, A.; Brolo, A. G.; Choo, J.; Cialla-May, D.; Deckert, V.; Fabris, L.; Faulds, K.; García de Abajo, F. J.; Goodacre, R.; Graham, D.; Haes, A. J.; Haynes, C. L.; Huck, C.; Itoh, T.; Käll, M.; Kneipp, J.; Kotov, N. A.; Kuang, H.; Le Ru, E. C.; Lee, H. K.; Li, J.-F.; Ling, X. Y.; Maier, S. A.; Mayerhöfer, T.; Moskovits, M.; Murakoshi, K.; Nam, J.-M.; Nie, S.; Ozaki, Y.; Pastoriza-Santos, I.; Perez-Juste, J.; Popp, J.; Pucci, A.; Reich, S.; Ren, B.; Schatz, G. C.; Shegai, T.; Schlücker, S.; Tay, L.-L.; Thomas, K. G.; Tian, Z.-Q.; Van Duyne, R. P.; Vo-Dinh, T.; Wang, Y.; Willets, K. A.; Xu, C.; Xu, H.; Xu, Y.; Yamamoto, Y. S.; Zhao, B.;

Liz-Marzán, L. M. Present and Future of Surface-Enhanced Raman Scattering. *ACS Nano* **2020**, *14*, 28−117.
(6) Fornasaro, S.; Alsamad, F.; Baia, M.; Batista de Carvalho, L. A. E.; Beleites, C.; Byrne, H. J.; Chiadò, A.; Chis, M.; Chisanga, M.; Daniel, A.; Dybas, J.; Eppe, G.; Falgayrac, G.; Faulds, K.; Gebavi, H.; Giorgis, F.; Goodacre, R.; Graham, D.; La Manna, P.; Laing, S.; Litti, L.; Lyng, F. M.; Malek, K.; Malherbe, C.; Marques, M. P. M.; Meneghetti, M.; Mitri, E.; Mohaček-Grošev, V.; Morasso, C.; Muhamadali, H.; Musto, P.; Novara, C.; Pannico, M.; Penel, G.; Piot, O.; Rindzevicius, T.; Rusu, E. A.; Schmidt, M. S.; Sergo, V.; Sockalingum, G. D.; Untereiner, V.; Vanna, R.; Wiercigroch, E.; Bonifacio, A. Surface Enhanced Raman Spectroscopy for Quantitative Analysis: Results of a Large-Scale European Multi-Instrument Interlaboratory Study. *Anal. Chem.* **2020**, *92*, 4053−4064.
(7) Litti, L.; Colusso, A.; Pinto, M.; Ruli, E.; Scarsi, A.; Ventura, L.; Toffoli, G.; Colombatti, M.; Fracasso, G.; Meneghetti, M. SERRS Multiplexing with Multivalent Nanostructures for the Identification and Enumeration of Epithelial and Mesenchymal Cells. *Sci. Rep.* **2020**, *10*, 15805.
(8) Joseph, V.; Matschulat, A.; Polte, J.; Rolf, S.; Emmerling, F.; Kneipp, J. SERS Enhancement of Gold Nanospheres of Defined Size. *J. Raman Spectrosc.* **2011**, *42*, 1736−1742.
(9) Farcau, C.; Astilean, S. Mapping the SERS Efficiency and Hot-Spots Localization on Gold Film over Nanospheres Substrates. *J. Phys. Chem. C* **2010**, *114*, 11717−11722.
(10) Smitha, S. L.; Gopchandran, K. G.; Ravindran, T. R.; Prasad, V. S. Gold Nanorods with Finely Tunable Longitudinal Surface Plasmon Resonance as SERS Substrates. *Nanotechnology* **2011**, *22*, 265705.
(11) Fu, G.; Sun, D. W.; Pu, H.; Wei, Q. Fabrication of Gold Nanorods for SERS Detection of Thiabendazole in Apple. *Talanta* **2019**, *195*, 841−849.
(12) Meng, X.; Dyer, J.; Huo, Y.; Jiang, C. Greater SERS Activity of Ligand-Stabilized Gold Nanostars with Sharp Branches. *Langmuir* **2020**, *36*, 3558−3564.
(13) He, S.; Kang, M. W. C.; Khan, F. J.; Tan, E. K. M.; Reyes, M. A.; Kah, J. C. Y. Optimizing Gold Nanostars as a Colloid-Based Surface-Enhanced Raman Scattering (SERS) Substrate. *J. Opt.* **2015**, *17*, 114013.
(14) Scarabelli, L.; Coronado-Puchau, M.; Giner-Casares, J. J.; Langer, J.; Liz-Marzán, L. M. Monodisperse Gold Nanotriangles : Assembly , and Performance in Surface-Enhanced Raman Scattering. *ACS Nano* **2014**, *8*, 5833−5842.
(15) Koetz, J. The Effect of Surface Modification of Gold Nanotriangles for Surface-Enhanced Raman Scattering Performance. *Nanomaterials* **2020**, *10*, 2187.
(16) Wang, X.; Wu, Y.; Wen, X.; Bai, X.; Qi, Y.; Zhang, L.; Yang, H.; Yi, Z. Composite Structure of Au Film/PMMA Grating Coated with Au Nanocubes for SERS Substrate. *Opt. Mater.* **2021**, *121*, 111536.
(17) Gao, Y.; Li, Y.; Wang, Y.; Chen, Y.; Gu, J.; Zhao, W.; Ding, J.; Shi, J. Controlled Synthesis of Multilayered Gold Nanoshells for Enhanced Photothermal Therapy and SERS Detection. *Small* **2015**, *11*, 77−83.
(18) Niu, R.; Song, C.; Gao, F.; Fang, W.; Jiang, X.; Ren, S.; Zhu, D.; Su, S.; Chao, J.; Chen, S.; Fan, C.; Wang, L. DNA Origami-Based Nanoprinting for the Assembly of Plasmonic Nanostructures with Single-Molecule Surface-Enhanced Raman Scattering. *Angew. Chem., Int. Ed.* **2021**, *60*, 11695−11701.
(19) Zhan, P.; Wen, T.; Wang, Z. G.; He, Y.; Shi, J.; Wang, T.; Liu, X.; Lu, G.; Ding, B. DNA Origami Directed Assembly of Gold Bowtie Nanoantennas for Single-Molecule Surface-Enhanced Raman Scattering. *Angew. Chem., Int. Ed.* **2018**, *57*, 2846−2850.
(20) Neto, D. M. A.; Rocha, J. S.; Fechine, P. B. A.; Vivas, L.; Singh, D. P.; Freire, R. M. Magnetic Nanoparticles in Analytical Chemistry. *Mater. Res. Proc.* **2020**, *66*, 173−216.
(21) Kelley, S. O.; Mirkin, C. A.; Walt, D. R.; Ismagilov, R. F.; Toner, M.; Sargent, E. H. Advancing the Speed, Sensitivity and Accuracy of Biomolecular Detection Using Multi-Length-Scale Engineering. *Nat. Nanotechnol.* **2014**, *9*, 969−980.
(22) Lai, H.; Xu, F.; Wang, L. A Review of the Preparation and Application of Magnetic Nanoparticles for Surface-Enhanced Raman Scattering. *J. Mater. Sci.* **2018**, *53*, 8677−8698.
(23) Litti, L.; Trivini, S.; Ferraro, D.; Reguera, J. 3D Printed Microfluidic Device for Magnetic Trapping and SERS Quantitative Evaluation of Environmental and Biomedical Analytes. *ACS Appl. Mater. Interfaces* **2021**, *13*, 34752−34761.
(24) Reguera, J.; Jiménez de Aberasturi, D.; Henriksen-Lacey, M.; Langer, J.; Espinosa, A.; Szczupak, B.; Wilhelm, C.; Liz-Marzán, L. M. Janus Plasmonic-Magnetic Gold-Iron Oxide Nanoparticles as Contrast Agents for Multimodal Imaging. *Nanoscale* **2017**, *9*, 9467−9480.
(25) Xu, X.; Li, H.; Hasan, D.; Ruoff, R. S.; Wang, A. X.; Fan, D. L. Near-Field Enhanced Plasmonic-Magnetic Bifunctional Nanotubes for Single Cell Bioanalysis. *Adv. Funct. Mater.* **2013**, *23*, 4332−4338.
(26) Tran, L. T. C.; Lesieur, S.; Faivre, V. Janus Nanoparticles: Materials, Preparation and Recent Advances in Drug Delivery. *Expet Opin. Drug Deliv.* **2014**, *11*, 1061−1074.
(27) Crossley, S.; Faria, J.; Shen, M.; Resasco, D. E. Solid Nanoparticles That Catalyze Biofuel Upgrade Reactions at the Water/Oil Interface. *Science* **2010**, *327*, 68−72.
(28) Zhai, Y.; Zhai, J.; Wang, Y.; Guo, S.; Ren, W.; Dong, S. Fabrication of Iron Oxide Core/Gold Shell Submicrometer Spheres with Nanoscale Surface Roughness for Efficient Surface-Enhanced Raman Scattering. *J. Phys. Chem. C* **2009**, *113*, 7009−7014.
(29) Qiu, Y.; Deng, D.; Deng, Q.; Wu, P.; Zhang, H.; Cai, C. Synthesis of Magnetic Fe3O4-Au Hybrids for Sensitive SERS Detection of Cancer Cells at Low Abundance. *J. Mater. Chem. B* **2015**, *3*, 4487−4495.
(30) Xie, Y.; Chen, T.; Guo, Y.; Cheng, Y.; Qian, H.; Yao, W. Rapid SERS Detection of Acid Orange II and Brilliant Blue in Food by Using Fe 3 O 4 @Au Core−Shell Substrate. *Food Chem.* **2019**, *270*, 173−180.
(31) Bhana, S.; Chaffin, E.; Wang, Y.; Mishra, S. R.; Huang, X. Capture and Detection of Cancer Cells in Whole Blood with Magnetic-Optical Nanoovals. *Nanomedicine* **2014**, *9*, 593−606.
(32) He, H.; Sun, D. W.; Pu, H.; Huang, L. Bridging Fe3O4@Au Nanoflowers and Au@Ag Nanospheres with Aptamer for Ultra-sensitive SERS Detection of Aflatoxin B1. *Food Chem.* **2020**, *324*, 126832.
(33) Bedford, E. E.; Méthivier, C.; Pradier, C. M.; Gu, F.; Boujday, S. Nanostructured and Spiky Gold Shell Growth on Magnetic Particles for Sers Applications. *Nanomaterials* **2020**, *10*, 2136.
(34) Quaresma, P.; Osório, I.; Dória, G.; Carvalho, P. A.; Pereira, A.; Langer, J.; Araújo, J. P.; Pastoriza-Santos, I.; Liz-Marzán, L. M.; Franco, R.; Baptista, P. V.; Pereira, E. Star-Shaped Magnetite@gold Nanoparticles for Protein Magnetic Separation and SERS Detection. *RSC Adv.* **2014**, *4*, 3690−3698.
(35) Tamer, U.; Onay, A.; Ciftci, H.; Bozkurt, A. G.; Cetin, D.; Suludere, Z.; Hakkı Boyacı, İ.; Daniel, P.; Lagarde, F.; Yaacoub, N.; Greneche, J. M. High-Yield Aqueous Synthesis of Multi-Branched Iron Oxide Core−Gold Shell Nanoparticles: SERS Substrate for Immobilization and Magnetic Separation of Bacteria. *J. Nanoparticle Res.* **2014**, *16*, 2624.
(36) Bhana, S.; Lin, G.; Wang, L.; Starring, H.; Mishra, S. R.; Liu, G.; Huang, X. Near-Infrared-Absorbing Gold Nanopopcorns with Iron Oxide Cluster Core for Magnetically Amplified Photothermal and Photodynamic Cancer Therapy. *ACS Appl. Mater. Interfaces* **2015**, *7*, 11637−11647.
(37) Fan, Z.; Senapati, D.; Khan, S. A.; Singh, A. K.; Hamme, A.; Yust, B.; Sardar, D.; Ray, P. C. Popcorn-Shaped Magnetic Core-Plasmonic Shell Multifunctional Nanoparticles for the Targeted Magnetic Separation and Enrichment, Label-Free SERS Imaging, and Photothermal Destruction of Multidrug-Resistant Bacteria. *Chem.—Eur. J.* **2013**, *19*, 2839−2847.
(38) Pinheiro, P. C.; Fateixa, S.; Nogueira, H. I. S.; Trindade, T. Magnetite-Supported Gold Nanostars for the Uptake and SERS Detection of Tetracycline. *Nanomaterials* **2019**, *9*, 31.

https://doi.org/10.1021/acsomega.2c06099
ACS Omega 2022, 7, 45493−45503

(39) Zhao, X.; Zeng, L.; Hosmane, N.; Gong, Y.; Wu, A. Cancer Cell Detection and Imaging: MRI-SERS Bimodal Splat-Shaped Fe3O4/Au Nanocomposites. *Chin. Chem. Lett.* **2019**, *30*, 87−89.
(40) Lai, H.; Shang, W.; Yun, Y.; Chen, D.; Wu, L.; Xu, F. Uniform Arrangement of Gold Nanoparticles on Magnetic Core Particles with a Metal-Organic Framework Shell as a Substrate for Sensitive and Reproducible SERS Based Assays: Application to the Quantitation of Malachite Green and Thiram. *Microchim. Acta* **2019**, *186*, 144.
(41) Xue, T.; Wang, S.; Ou, G.; Li, Y.; Ruan, H.; Li, Z.; Ma, Y.; Zou, R.; Qiu, J.; Shen, Z.; Wu, A. Detection of Circulating Tumor Cells Based on Improved SERS-Active Magnetic Nanoparticles. *Anal. Methods* **2019**, *11*, 2918−2928.
(42) Sun, M.; Zhao, A.; Wang, D.; Wang, J.; Chen, P.; Sun, H. Cube-like Fe3O4@SiO2@Au@Ag Magnetic Nanoparticles: A Highly Efficient SERS Substrate for Pesticide Detection. *Nanotechnology* **2018**, *29*, 165302.
(43) Han, D.; Li, B.; Chen, Y.; Wu, T.; Kou, Y.; Xue, X.; Chen, L.; Liu, Y.; Duan, Q. Facile Synthesis of Fe3O4@Au Core-Shell Nanocomposite as a Recyclable Magnetic Surface Enhanced Raman Scattering Substrate for Thiram Detection. *Nanotechnology* **2019**, *30*, 465703.
(44) Chen, P.; Zhao, A.; Wang, J.; He, Q.; Sun, H.; Wang, D.; Sun, M.; Guo, H. In-Situ Monitoring Reversible Redox Reaction and Circulating Detection of Nitrite via an Ultrasensitive Magnetic Au@Ag SERS Substrate. *Sensor. Actuator. B Chem.* **2018**, *256*, 107−116.
(45) Reguera, J.; Jiménez de Aberasturi, D.; Winckelmans, N.; Langer, J.; Bals, S.; Liz-Marzán, L. M. Synthesis of Janus Plasmonic-Magnetic, Star-Sphere Nanoparticles, and Their Application in SERS Detection. *Faraday Discuss.* **2016**, *191*, 47−59.
(46) Shen, J.; Zhu, Y.; Yang, X.; Zong, J.; Li, C. Multifunctional Fe 3 O 4 @ Ag / SiO 2 / Au Core − Shell Microspheres as a Novel SERS-Activity Label via Long-Range Plasmon Coupling. *Langmuir* **2013**, *29*, 690−695.
(47) Li, Y.; Zhao, J.; You, W.; Cheng, D.; Ni, W. Gold Nanorod@iron Oxide Core-Shell Heterostructures: Synthesis, Characterization, and Photocatalytic Performance. *Nanoscale* **2017**, *9*, 3925−3933.
(48) Mezni, A.; Balti, I.; Mlayah, A.; Jouini, N.; Smiri, L. S. Hybrid Au-Fe3O4 Nanoparticles: Plasmonic, Surface Enhanced Raman Scattering, and Phase Transition Properties. *J. Phys. Chem. C* **2013**, *117*, 16166−16174.
(49) Hong, W. E.; Hsu, I. L.; Huang, S. Y.; Lee, C. W.; Ko, H.; Tsai, P. J.; Shieh, D. B.; Huang, C. C. Assembled Growth of 3D Fe3O4@Au Nanoparticles for Efficient Photothermal Ablation and SERS Detection of Microorganisms. *J. Mater. Chem. B* **2018**, *6*, 5689−5697.
(50) Pinheiro, P. C.; Fateixa, S.; Trindade, T. Sers Detection of Penicillin g Using Magnetite Decorated with Gold Nanoparticles. *Magnetochemistry* **2017**, *3*, 32.
(51) Gan, Z.; Zhao, A.; Zhang, M.; Wang, D.; Guo, H.; Tao, W.; Gao, Q.; Mao, R.; Liu, E. Fabrication and Magnetic-Induced Aggregation of Fe3O 4-Noble Metal Composites for Superior SERS Performances. *J. Nanoparticle Res.* **2013**, *15*, 1954.
(52) Wang, L. P.; Huang, Y. B.; Lai, Y. H. Surface Enhanced Raman Scattering Activity of Dual-Functional Fe 3 O 4 /Au Composites. *Appl. Surf. Sci.* **2018**, *435*, 290−296.
(53) Zhang, H.; Yi, Y.; Zhou, C.; Ying, G.; Zhou, X.; Fu, C.; Zhu, Y.; Shen, Y. SERS Detection of MicroRNA Biomarkers for Cancer Diagnosis Using Gold-Coated Paramagnetic Nanoparticles to Capture SERS-Active Gold Nanoparticles. *RSC Adv.* **2017**, *7*, 52782−52793.
(54) Maurer, V.; Frank, C.; Porsiel, J. C.; Zellmer, S.; Garnweitner, G.; Stosch, R. Step-by-Step Monitoring of a Magnetic and SERS-Active Immunosensor Assembly for Purification and Detection of Tau Protein. *J. Biophot.* **2020**, *13*, 1−10.
(55) Ding, Q.; Zhou, H.; Zhang, H.; Zhang, Y.; Wang, G.; Zhao, H. 3D Fe3O4@Au@Ag Nanoflowers Assembled Magnetoplasmonic Chains for: In Situ SERS Monitoring of Plasmon-Assisted Catalytic Reactions. *J. Mater. Chem. A* **2016**, *4*, 8866−8874.
(56) Büchner, T.; Drescher, D.; Merk, V.; Traub, H.; Guttmann, P.; Werner, S.; Jakubowski, N.; Schneider, G.; Kneipp, J. Biomolecular Environment, Quantification, and Intracellular Interaction of Multifunctional Magnetic SERS Nanoprobes. *Analyst* **2016**, *141*, 5096−5106.
(57) La Porta, A.; Sánchez-Iglesias, A.; Altantzis, T.; Bals, S.; Grzelczak, M.; Liz-Marzán, L. M. Multifunctional Self-Assembled Composite Colloids and Their Application to SERS Detection. *Nanoscale* **2015**, *7*, 10377−10381.
(58) Mo, A. H.; Landon, P. B.; Gomez, K. S.; Kang, H.; Lee, J.; Zhang, C.; Janetanakit, W.; Sant, V.; Lu, T.; Colburn, D. A.; Akkiraju, S.; Dossou, S.; Cao, Y.; Lee, K. F.; Varghese, S.; Glinsky, G.; Lal, R. Magnetically-Responsive Silica-Gold Nanobowls for Targeted Delivery and SERS-Based Sensing. *Nanoscale* **2016**, *8*, 11840−11850.
(59) Chen, P. J.; Kang, Y. D.; Lin, C. H.; Chen, S. Y.; Hsieh, C. H.; Chen, Y. Y.; Chiang, C. W.; Lee, W.; Hsu, C. Y.; Liao, L. D.; Fan, C. T.; Li, M. L.; Shyu, W. C. Multitheragnostic Multi-GNRs Crystal-Seeded Magnetic Nanoseaurchin for Enhanced in Vivo Mesenchymal-Stem-Cell Homing, Multimodal Imaging, and Stroke Therapy. *Adv. Mater.* **2015**, *27*, 6488−6495.
(60) Maurer, V.; Zarinwall, A.; Wang, Z.; Wundrack, S.; Wundrack, N.; Ag Seleci, D.; Helm, V.; Otenko, D.; Frank, C.; Schaper, F.; Stosch, R.; Garnweitner, G. All-in-One Superparamagnetic and SERS-Active Niosomes for Dual-Targeted in Vitro Detection of Breast Cancer Cells. *Sens. Diagn.* **2022**, *1*, 469−484.
(61) Ding, G.; Xie, S.; Zhu, Y.; Liu, Y.; Wang, L.; Xu, F. Graphene Oxide Wrapped Fe3O4@Au Nanohybrid as SERS Substrate for Aromatic Dye Detection. *Sensor. Actuator. B Chem.* **2015**, *221*, 1084−1093.
(62) Rincón-Iglesias, M.; Rodrigo, I.; Berganza, L. B.; Serea, E. S. A.; Plazaola, F.; Lanceros-Méndez, S.; Lizundia, E.; Reguera, J. Core-Shell Fe3O4@Au Nanorod-Loaded Gels for Tunable and Anisotropic Magneto- and Photothermia. *ACS Appl. Mater. Interfaces* **2022**, *14*, 7130−7140.
(63) Wang, H.; Brandl, D. W.; Le, F.; Nordlander, P.; Halas, N. J. Nanorice: A Hybrid Plasmonic Nanostructure. *Nano Lett.* **2006**, *6*, 827−832.
(64) Yang, Y.; Huang, M.; Qian, J.; Gao, D.; Liang, X. Tunable Fe3O4 Nanorods for Enhanced Magnetic Hyperthermia Performance. *Sci. Rep.* **2020**, *10*, 8331.
(65) Kloust, H.; Zierold, R.; Merkl, J. P.; Schmidtke, C.; Feld, A.; Pöselt, E.; Kornowski, A.; Nielsch, K.; Weller, H. Synthesis of Iron Oxide Nanorods Using a Template Mediated Approach. *Chem. Mater.* **2015**, *27*, 4914−4917.
(66) Michota, A.; Bukowska, J. Surface-Enhanced Raman Scattering (SERS) of 4-Mercaptobenzoic Acid on Silver and Gold Substrates. *J. Raman Spectrosc.* **2003**, *34*, 21−25.
(67) Pilot, R. SERS Detection of Food Contaminants by Means of Portable Raman Instruments. *J. Raman Spectrosc.* **2018**, *49*, 954−981.
(68) Mason, D. J.; Power, E. G. M.; Talsania, H.; Phillips, I.; Gant, V. A. Antibacterial Action of Ciprofloxacin. *Antimicrob. Agents Chemother.* **1995**, *39*, 2752−2758.
(69) Silva, A. R.; Martins, P. M.; Teixeira, S.; Carabineiro, S. A. C.; Kuehn, K.; Cuniberti, G.; Alves, M. M.; Lanceros-Mendez, S.; Pereira, L. Ciprofloxacin Wastewater Treated by UVA Photocatalysis: Contribution of Irradiated TiO2 and ZnO Nanoparticles on the Final Toxicity as Assessed by Vibrio Fischeri. *RSC Adv.* **2016**, *6*, 95494−95503.
(70) Baquero, F.; Martínez, J. L.; Cantón, R. Antibiotics and Antibiotic Resistance in Water Environments. *Curr. Opin. Biotechnol.* **2008**, *19*, 260−265.
(71) Al-Buriahi, A. K.; Al-shaibani, M. M.; Mohamed, R. M. S. R.; Al-Gheethi, A. A.; Sharma, A.; Ismail, N. Ciprofloxacin Removal from Non-Clinical Environment: A Critical Review of Current Methods and Future Trend Prospects. *J. Water Proc. Eng.* **2022**, *47*, 102725.
(72) Xiong, J. Q.; Kurade, M. B.; Kim, J. R.; Roh, H. S.; Jeon, B. H. Ciprofloxacin Toxicity and Its Co-Metabolic Removal by a Freshwater Microalga Chlamydomonas Mexicana. *J. Hazard. Mater.* **2017**, *323*, 212−219.
(73) Hohenester, U. Making Simulations with the MNPBEM Toolbox Big: Hierarchical Matrices and Iterative Solvers. *Comput. Phys. Commun.* **2018**, *222*, 209−228.

https://doi.org/10.1021/acsomega.2c06099
ACS Omega 2022, 7, 45493−45503

(74) Piotto, V.; Litti, L.; Meneghetti, M. Synthesis and Shape Manipulation of Anisotropic Gold Nanoparticles by Laser Ablation in Solution. *J. Phys. Chem. C* **2020**, *124*, 4820−4826.
(75) Litti, L.; Meneghetti, M. Predictions on the SERS Enhancement Factor of Gold Nanosphere Aggregate Samples. *Phys. Chem. Chem. Phys.* **2019**, *21*, 15515−15522.
(76) Piotto, V.; Litti, L.; Omelyanchik, A.; Martucci, A.; Riello, P.; Peddis, D.; Meneghetti, M. Synthesis of Magnetic Nanoparticles by Laser Ablation of Strontium Ferrite under Water and Their Characterization by Optically Detected Magnetophoresis Supported by BEM Calculations. *J. Mater. Chem. C* **2022**, *10*, 3819−3825.
(77) Crut, A.; Maioli, P.; Del Fatti, N.; Vallée, F. Optical Absorption and Scattering Spectroscopies of Single Nano-Objects. *Chem. Soc. Rev.* **2014**, *43*, 3921−3956.
(78) Prodan, E.; Radloff, C.; Halas, N. J.; Nordlander, P. A Hybridization Model for the Plasmon Response of Complex Nanostructures. *Science* **2003**, *302*, 419−422.
(79) Stauffer, M. T.*Applications of Molecular Spectroscopy to Current Research in the Chemical and Biological Sciences*; IntechOpen, 2016.
(80) Hendel, T.; Wuithschick, M.; Kettemann, F.; Birnbaum, A.; Rademann, K.; Polte, J. In Situ Determination of Colloidal Gold Concentrations with UV-Vis Spectroscopy: Limitations and Perspectives. *Anal. Chem.* **2014**, *86*, 11115−11124.
(81) Reich, D. H.; Tanase, M.; Hultgren, A.; Bauer, L. A.; Chen, C. S.; Meyer, G. J. Biological Applications of Multifunctional Magnetic Nanowires (Invited). *J. Appl. Phys.* **2003**, *93*, 7275−7280.
(82) Lee, A.; Andrade, G. F. S.; Ahmed, A.; Souza, M. L.; Coombs, N.; Tumarkin, E.; Liu, K.; Gordon, R.; Brolo, A. G.; Kumacheva, E. Probing Dynamic Generation of Hot-Spots in Self-Assembled Chains of Gold Nanorods by Surface-Enhanced Raman Scattering. *J. Am. Chem. Soc.* **2011**, *133*, 7563−7570.
(83) Halas, N. J.; Lal, S.; Chang, W. S.; Link, S.; Nordlander, P. Plasmons in Strongly Coupled Metallic Nanostructures. *Chem. Rev.* **2011**, *111*, 3913−3961.
(84) Lee, D. K.; Song, Y.; Tran, V. T.; Kim, J.; Park, E. Y.; Lee, J. Preparation of Concave Magnetoplasmonic Core-Shell Supraparticles of Gold-Coated Iron Oxide via Ion-Reducible Layer-by-Layer Method for Surface Enhanced Raman Scattering. *J. Colloid Interface Sci.* **2017**, *499*, 54−61.
(85) Marti, E.; Huerta, B.; Rodríguez-Mozaz, S.; Barceló, D.; Balcázar, J. L.; Marcé, R. Effects of Subinhibitory Ciprofloxacin Concentrations on the Abundance of QnrS and Composition of Bacterial Communities from Water Supply Reservoirs. *Chemosphere* **2016**, *161*, 470−474.
(86) Shen, R.; Yu, Y.; Lan, R.; Yu, R.; Yuan, Z.; Xia, Z. The Cardiovascular Toxicity Induced by High Doses of Gatifloxacin and Ciprofloxacin in Zebrafish. *Environ. Pollut.* **2019**, *254*, 112861.
(87) Robinson, A. A.; Belden, J. B.; Lydy, M. J. Toxicity of Fluoroquinolone Antibiotics to Aquatic Organisms. *Environ. Toxicol. Chem.* **2005**, *24*, 423−430.
(88) Martins, N.; Pereira, R.; Abrantes, N.; Pereira, J.; Gonçalves, F.; Marques, C. R. Ecotoxicological Effects of Ciprofloxacin on Freshwater Species: Data Integration and Derivation of Toxicity Thresholds for Risk Assessment. *Ecotoxicology* **2012**, *21*, 1167−1176.
(89) Johnson, A. C.; Keller, V.; Dumont, E.; Sumpter, J. P. Assessing the Concentrations and Risks of Toxicity from the Antibiotics Ciprofloxacin, Sulfamethoxazole, Trimethoprim and Erythromycin in European Rivers. *Sci. Total Environ.* **2015**, *511*, 747−755.

https://doi.org/10.1021/acsomega.2c06099
ACS Omega 2022, 7, 45493−45503